RESEARCH ARTICLE

Jamming Gripper-Inspired Soft Jig for Perceptive Parts Fixing

TATSUYA SAKUMA [1], (Member, IEEE), TAKUYA KIYOKAWA [1,2], (Member, IEEE),
TAKAMITSU MATSUBARA [1], (Member, IEEE), JUN TAKAMATSU[3], (Member, IEEE),
TAKAHIRO WADA [1], (Member, IEEE), AND TSUKASA OGASAWARA [4], (Life Member, IEEE)

[1]Division of Information Science, Graduate School of Science and Technology, Nara Institute of Science and Technology, Ikoma 630-0192, Japan
[2]Department of Systems Innovation, Graduate School of Engineering Science, Osaka University, Osaka 565-0871, Japan
[3]Microsoft, Redmond, WA 98052, USA
[4]Institute for Research Initiatives, Nara Institute of Science and Technology, Ikoma 630-0192, Japan

Corresponding author: Tatsuya Sakuma (sakuma.tatsuya.sn1@is.naist.jp)

ABSTRACT To achieve precise and time-efficient operation to ensure stable and reliable product assembly, custom-made jigs have been developed for each assembly part. However, designing these jigs is a time-consuming task. Therefore, this study proposes a jamming gripper-inspired flexible jig using a soft membrane consisting of transparent beads and oil with an adjusted refractive index. The proposed jig is equipped with a hydraulic drive system with visual control of the amount of transparent oil inside the jig. The proposed system enables parts fixing by creating a jammed state while maintaining optical transparency, thereby facilitating the visual sensing of the jig's membrane from camera sensors embedded in the jig. Furthermore, a sensing method was developed to perform a precise assembly without external sensors to estimate the pose of an object based on the proposed point-to-function iterative closest point. The results show that the proposed system successfully estimates the orientation at a root mean square error of less than 4° when the position is varied from 0 mm to 20 mm and the angle is varied from 0° to 20°. Furthermore, it can repeatedly fix the object in any orientation from 0° to 20° at a position of less than 0.5 mm and an angle of less than 1.1°.

INDEX TERMS Flexible manufacturing systems, robotic assembly, soft robotics, vision sensors.

I. INTRODUCTION

In robotic assembly processes, jigs play a critical role in achieving precise assembly by fixing objects in desired poses. Positioning the target object with a jig designed based on the object shape facilitates precise and efficient robotic assembly [1]. However, because the jig prepared for a particular object is not applicable to other objects, the jig must be redesigned each time the manufacturing object changes, resulting in cost and time loss. This study aims to address the issue by developing a general-purpose jig that can achieve high-mix, low-volume production quickly and cost-effectively.

The general-purpose jig should be designed to position and constrain the object even if there is a positioning error in the robot [2]. A vise is a well-known general-purpose
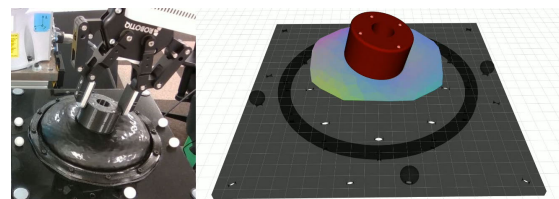
FIGURE 1. Left: Soft jig with a thin and soft membrane and transparent beads and oil. Right: Pose estimation result.

jig that fixes objects based on clamping force. General-purpose jigs with improved object adaptability include pin-array jigs [3], [4], [5] and jamming jigs [6]. Fig. 2 compares the contact points, flexibility, and sensing ability of general-purpose jigs.

The jig has at least two contact points consisting of a locator or a clamp that constrain the object. The more contact points, the more versatile the object that can be handled
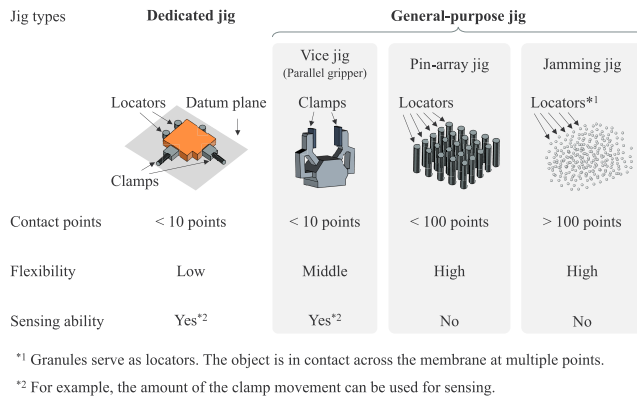
FIGURE 2. Comparison of contact points, flexibility, and sensing ability of general-purpose jigs.

because it can constrain the shape of the object. However, if there are many contact points, the number of contact points that must be measured to determine the constraining state of an object increases, reducing the ease of sensing.

To solve this trade-off problem, we investigated a method for acquiring object orientation with a jamming jig with many contact points.

Although it is possible to estimate the object pose fixed on the jig using vision-based perception techniques [7], [8], the direction other than the bottom surface that contacts the jig should be unobstructed by sensors to allow the robot to approach the part from various perspectives. Therefore, incorporating an internal sensing system into the jig can provide a more reliable solution that is accessible to the robot and has sensing ability.

This paper proposes a new two-in-one flexible jig (called a soft jig) that provides flexibility to fix various objects and the sensing ability to perceive the pose of a fixed object. The soft jig fixes an object by utilizing particle jamming, which evacuates the inner fluid inside the jig; this technique is famously used in a jamming gripper [9]. Furthermore, the soft jig can estimate the pose of a fixed object by acquiring the shape of the deformed membrane based on optical sensing. Because there is always a contact surface when fixing an object, if the pose can be estimated using this surface, the object-fixing and estimation can be completed using the jig alone.

Based on our previous studies, we used transparent beads and replaced the air used for the jamming grippers with transparent oil that had a refractive index close to that of the beads; this allows optical sensing under the jamming mechanism [10], [11]. If the refractive indices of all materials inside the jig are similar, the surface of the membrane can be captured optically by the camera when light travels straight through. Markers were painted on the inner surface of the membrane, and two cameras were installed inside the jig to convert the captured image into the shape of the membrane. Furthermore, we used a hydraulic drive system with visual control of the amount of transparent oil inside the jig. If the

amount of oil discharged is not adequate when controlling the pump, bubbles will be generated, and the membrane on the jig will not be visible from the sensor as described in Appendix A.

This study estimates the object position and orientation based on a proposed point-to-function iterative closest point (ICP) that finds a transformation from the reconstructed membrane surface to the bottom surface of the object model. More specifically, we detect the markers on the membrane, estimate the marker positions, represent a curved surface from the markers, and determine the object pose with the transformation, as shown in Fig. 1. Using this approach, we estimated the object's orientation at a root mean square error (RMSE) of less than 4° for positions from 0 mm to 20 mm and angles from 0° to 20°.

In summary, our primary contributions are as follows:

- A design for a flexible assembly jig to achieve the object pose estimation and parts fixing (Section III).
- A hydraulic drive system with visual-based control of the amount of transparent oil inside the jig, which facilitates the creation of a jammed state for parts fixing while maintaining optical transparency (Section IV-A).
- A sensing method for estimating object poses fixed on the jig by utilizing point-to-function ICP (Sections IV-B and IV-C).

II. RELATED WORK

A. FLEXIBLE JIGS AND FIXTURES

Flexible jigs (fixtures) have been developed using various strategies. However, reducing the uncertainty of the fixed pose is an open issue in the previous strategies.

Reconfigurable jigs [12], [13], [14] fix objects and support their surfaces by rearranging or replacing multiple components according to the shape of the object. The ability to change a fixed configuration provides flexibility. Pin array jigs [3], [4], [5] use a shape-memorable mechanism to fix objects by constraining multiple points of an object with pins. When fixing components using pins, a high degree of freedom (DoF) facilitates flexibility. Flexible material jigs [6], [15] use elastomeric materials to deform the surface of the fixture depending on the object shapes to be fixed. In [6] and [15], parts fixing is accomplished by jamming transition and vacuum mechanisms.

Although flexible material jigs [6], [15] allow for versatile fixing compared to other flexible fixtures, the precision of the fixing in target poses is a disadvantage. One method for overcoming this issue is to utilize tactile sensing to reduce the uncertainty of a fixed pose.

B. TACTILE SENSING FOR SOFT ROBOTICS

Because a high spatial resolution enables high object pose estimation accuracy, we focus on camera-based methods.

GelSight [16] is a well-known tactile sensor that acquires a normal map for an object in contacting the sensor. The sensor utilizes multiple light sources of different colors to obtain the normal based on the photometric stereo. *SoftBubble* [17], [18]
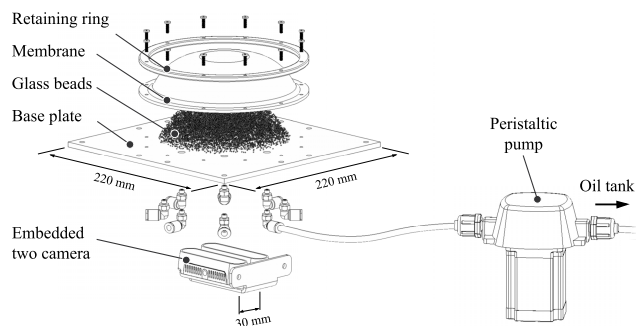
FIGURE 3. Design of the proposed soft jig. Note that the oil flow piping is simplified for clarity.
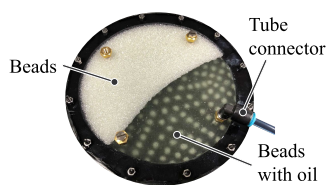
FIGURE 4. Appearance of the soft jig while being filled with oil, viewed from the camera side. Although the beads are packed tightly inside the membrane, the markers can be observed through the filling oil.

uses an air-inflated balloon to acquire the shape of the object with a depth camera through the balloon membrane. Lin et al. [19] proposed a sensor that estimates the curvature of a flexible material using the subtractive color-mixing principle. In our previous work, we developed a sensing jamming gripper that (1) grasps an object using transparent beads and oil for jamming-based grasping and (2) acquires the membrane shape using an embedded camera and markers of known sizes attached to the membrane [10], [11]. *TaTa* [20] is a soft gripper capable of sensing tactile information by incorporating the techniques of *GelSight* [16] into our previously developed jamming gripper [10].

The soft jig is designed to be larger than the sensing grippers [10], [20], and the area of contact with the object is increased by decreasing the size of the beads to be filled to achieve a parts fixing performance suitable for the jig. These design changes were expected to reduce the internal transparency and marker sensing accuracy in the previously proposed method. Nevertheless, the use of passive stereo with two cameras (in Section III) and the proposed image processing system for blurred images (in Section IV-B) helped overcome these problems to estimate the object pose.

III. DESIGN OF SOFT JIG

The soft jig, shown in Fig. 3, comprises the following five key components:

- A silicone membrane with markers to capture the surface deformation
- Glass beads for jamming transition
- A base plate cut out of transparent polyethylene terephthalate
- A pump to create a jammed state
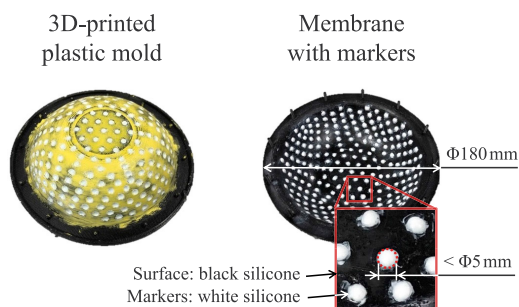
FIGURE 5. Mold (left) to fabricate the membrane (right) of the soft jig. The curved surface of the membrane can be formed by coating liquid silicone material onto a rigid mold.

- Two cameras to acquire the point cloud data around the target object using triangulation

The base plate size was 220mm × 220mm × 5mm, and the height of the silicone membrane was approximately 30 mm from the base plate. The pancake-like shape increases the robot's ability to reach the object from the top by preventing the object from sinking deeper in a hemispherical shape. As shown in Fig. 4, the soft jig was filled with oil inside the membrane, and the markers were observed even when the membrane was filled with beads.

A. SILICONE MEMBRANE

A silicone membrane with multiple rounded markers was formed using the mold shown in Fig. 5. The membrane thickness was less than 1 mm (approximately 0.7 mm). To form a thin membrane that easily deformed to assume the shape of the object, we employed a method for coating liquid silicone rubber (Dragon Skin FX-Pro, Smooth-On) on a mold surface instead of casting the material with several molds. The mold had hemispherical indentations to create markers, which in turn were filled with white silicone, which was colored with a pigment (Silc Pig, Smooth-On) and mixed with a thickener (THI-VEX, Smooth-On).

After the white silicone hardened, the black silicone adhered to the mold surface after filling the indentations. Instead of using the original color of the silicone, it was colored to allow easy detection of the marker during image processing. The mold was printed using a 3D printer. We removed the layer lines on the mold surface using polyester putty to allow easy removal of the hardened silicone from the 3D-printed plastic mold.

B. GLASS BEADS

If large beads and a thin membrane are used, the shape of the bead will cause bumps on the surface of the membrane; as a result, the contact between the membrane and the object changes from surface contact to point contact, decreasing the coefficient of friction between the object and the membrane [21]. Therefore, beads covered with a silicone membrane should be small in diameter to avoid deteriorating the parts fixing performance. Furthermore, the beads must be
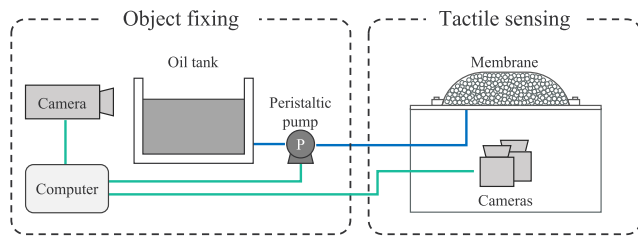
FIGURE 6. System configuration of the soft jig. The blue and green lines denote the oil flow tubes and electrical connections, respectively.

transparent to make the inner markers visible to the cameras. Based on these requirements, we selected 1 mm glass beads (FGB-20, Fuji Manufacturing).

C. BASE PLATE

The base plate must be transparent to make the membrane markers visible. It cannot allow leakage of the oil and beads inside and must allow only oil to be pumped through the connected tube.

To achieve this, the plate holds the silicone membrane and tube connectors. Tube connectors with a filter were attached to the underside of the base plate to pump the oil while preventing the beads from flowing out. Because of the small diameter of the beads, the filters must be finer, which reduces the cross-sectional area A required to enter the tube and the mass flow rate Q; this is indicated by the equation $Q = \rho A V$, where ρ is the oil density, A is the cross-sectional area, and V is the velocity. In a production line, it is necessary to increase Q to shorten the time. Eight tube connectors were attached to the base plate to distribute the filter load.

D. CAMERA

To acquire the deformation of the membrane, we used two cameras embedded inside the jig to capture a pair of images. The two cameras (RealSense D435, Intel) were placed approximately 150 mm under the base plate with a baseline of 30 mm.

Although RealSense D435 can be used to acquire point cloud data based on the active stereo method, the function cannot be used in this hardware configuration of the soft jig. This is because the infrared light projected from the camera is reflected by the transparent base plate without reaching the inner surface of the membrane.

To eliminate the influence of ambient light, the cameras were surrounded with black plastic plates, and light-emitting diode (LED) lights near the camera maintained a constant brightness during sensing.

IV. FIXING AND SENSING SYSTEM

Fig. 6 shows the system configuration of the soft jig. To achieve parts fixing and object-pose estimation, the system comprises three parts: an object-fixing part, a membrane shape-sensing part, and an object pose estimation part.

TABLE 1. Fluid actuation methods for jamming transition.

	Pneumatic-driven	Hydraulic-driven
Fluid type	Compressible fluid	Incompressible fluid
Actuators to drive	Compressor + ejector, vacuum pump + valve, etc.	Peristaltic pump, hydraulic cylinder + linear actuator, etc.
Advantages	Easiness of actuation	Improving the holding force [*1]
Disadvantages	–	Difficulty of actuation [*1] [*2]
Remarks	Does not allow optical sensing because of opaque filling	Can be combined with optical sensing because of transparent filling

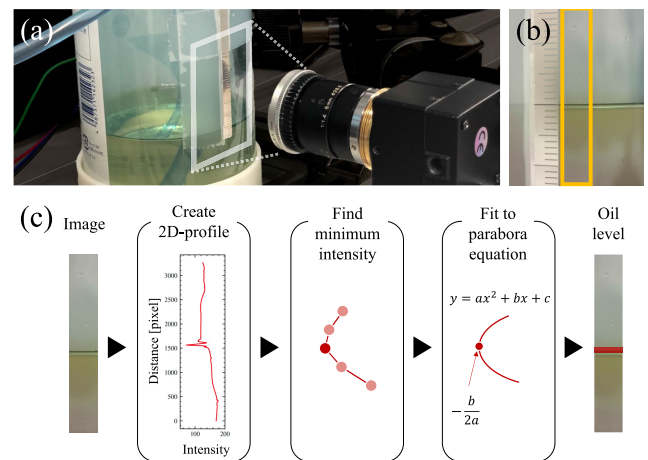[*1] are described in [22]
[*2] is described in Appendix A

FIGURE 7. (a) Setup of the oil tank and the external camera. (b) Appearance of the oil level from the external camera side. Oil level per pixel is approximately 10 μm. (c) Flowchart of the oil level measurement.

A. OBJECT-FIXING PART

To fix an object in the proposed jig, controlling the input and output of the fluid inside the membrane is necessary. Table 1 shows the difference between pneumatic and hydraulic drives for the jamming transition.

The advantage of the hydraulic-driven method is that it can be combined with optical sensing. It is challenging to perform optical sensing with the pneumatic-driven approach because no object has the same refractive index as air. However, the hydraulic-driven method requires precise control to prevent excessive input–output that causes cavitation and membrane breakage owing to the incompressibility of oil. Because cavitation inhibits the passage of light, it is prevented by precisely measuring the oil level of the tank and controlling the amount of oil using a peristaltic pump.

To achieve a highly precise oil-level measurement of less than 1 mm, which is unfeasible with commercially available level sensors, such as capacitive, conductive, or float sensors, a camera was used to capture the transparent oil tank from the side with a high resolution. This method allows for
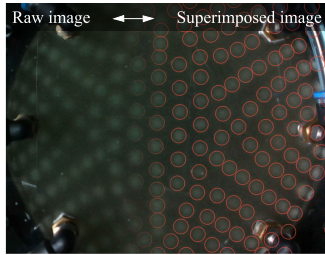
FIGURE 8. Appearance of markers on the inner surface of the soft jig when viewed from the camera side. The markers were blurred, making it challenging to determine their exact size; nevertheless, their positions could be captured. The red circles superimposed on the image result from marker detection by Laplacian of Gaussian (LoG).

greater precision in oil-level control using a peristaltic pump. On the other hand, the method of sensing oil pressure is not suitable for this application, as the pressure value may change regardless of the oil level inside the jig, for example, when it comes into contact with an object. Fig. 7 (a) shows the setup of the oil tank and external camera, and Fig. 7 (b) shows the actual captured image, where the yellow box represents the area for creating a two-dimensional profile. Fig. 7 (c) shows a flowchart of the oil-level measurement procedure. The oil level per pixel in an image is approximately 10 μm. The liquid surface is black because the oil rises on the wall surface by capillary action and appears similar to a concave cylindrical lens when viewed from the side.

First, a two-dimensional profile was created by averaging the pixel values in the yellow box in the horizontal direction to analyze the intensity values of the image with respect to the height direction of the tank. Second, the minimum intensity candidate was detected to convert the two-dimensional profile into an oil level measurement, considering that the liquid surface viewed from the side appeared black. To achieve sub-pixel accuracy in the oil level measurement, a parabola function was fitted on measured points around the minimum intensity candidate, and the minimum value with the fitted function was determined. This method enabled us to accurately measure the oil level in the tank.

The acquired oil level was used to control the jamming transition by driving the peristaltic pump until the target value was reached. Since the peristaltic pump was driven by a stepping motor, the system could control the amount of oil in response to the pulse input in a closed loop, using the oil level as a feedback parameter.

B. MEMBRANE SHAPE-SENSING

Fig. 8 shows the markers observed in the oil. The markers on the inner surface of the membrane were visible owing to the refractive index-tuned oil, although light travels through several beads to reach the membrane. Because the refractive index was adjusted by the human eye while changing the mixing ratio of paraffin and silicone oils, it did not perfectly match the glass beads and appeared blurred in the camera images.
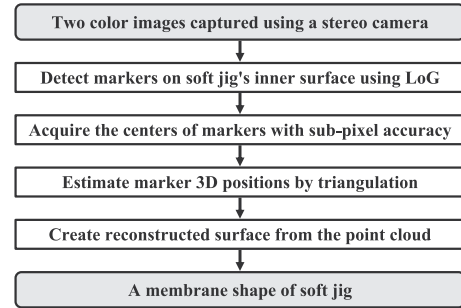
FIGURE 9. Flowchart of the proposed membrane shape-sensing. The inputs were two paired images, and the output was the pose of the object on the soft jig.
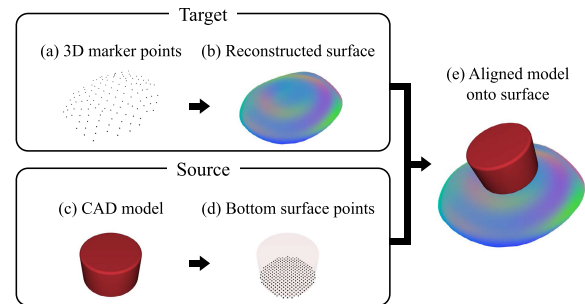
FIGURE 10. Point-to-function ICP that finds a transformation from the reconstructed membrane surface to the bottom surface of the object model.
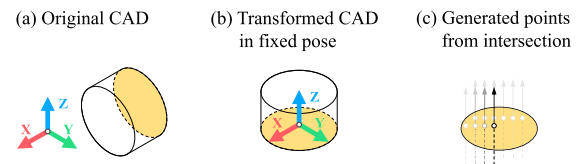

FIGURE 11. Pre-processing to convert a computer-aided design (CAD) model into points. (a) Original CAD model. The yellow surface is the bottom when fixed. (b) Transformed CAD model in the fixed pose coordinate system. (c) Generated points from the intersection of the z-up vector and the bottom surface.

Fig. 9 shows a flowchart of the proposed membrane shape-sensing that uses acquired images. The system captures a point cloud that represents the membrane shape from the image and treats it as a surface to acquire the membrane shape as a surface function.

LoG was used to accurately detect marker centers in blurred images. Using the known variation in the marker size in the image, σ of the Gaussian filter was determined, and the center of the markers was calculated by extracting the local maximum from the LoG image.

The centers of the markers detected in the left and right images were acquired in integer pixel units. To acquire the center with sub-pixel accuracy, a least-squares fitting is performed to a quadratic function in the x- and y-directions, respectively, using pixels in the neighborhood of the center. Subsequently, the marker centers were converted to the three-dimensional point cloud based on the triangulation method.
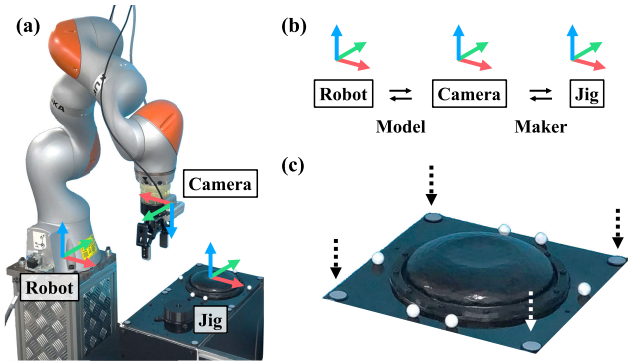
FIGURE 12. Experimental setup. (a) A manipulator is used to push the object in a fixed pose. (b) Transformation relationships for each coordinate. The transformation from the robot to the camera is computed using model information and kinematics. The transformation from the camera to the jig is computed using known camera parameters and marker placement. (c) Four white circular markers at the ends of the dotted arrows align the soft jig with the robot coordinates.

FIGURE 13. Three cylindrical objects with different diameters: 30 mm, 50 mm, and 80 mm. All objects have the same height of 30 mm.

FIGURE 14. Illustration of the motion of the robot to press the object against the jig.

The acquired point cloud is equivalent to the bottom surface of the contacting object. Owing to the soft membrane, the object shape appeared on the membrane as a continuous curved surface smoothed from its original shape owing to the uniform distribution of the fluid. When the object is pressed against the membrane, the membrane enclosing the fluid maintains its surface as a smooth curve. Because a point cloud is a continuous curved surface, it can be defined as a differentiable surface function using the radial basis function. This allows interpolation of the surface heights and normals at any xy-position.

C. OBJECT POSE ESTIMATION

Fig. 10 shows the point-to-function ICP, the proposed algorithm for estimating the orientation of a pushed object. Fig. 11 shows a point cloud of the bottom surface generated using the CAD model as the source for the pose estimation. The coordinate system of the CAD model is adjusted to the fixing pose, and the intersection points with the z-up vector are calculated by shifting the xy-position of the z-up vector at regular pitch intervals. The lowest value in the intersection area is treated as the bottom surface point.

The pose of the object is estimated by performing ICP using a CAD point cloud and a differentiable surface function. In point-to-plane ICP, the source and target point clouds are static, and the pair points of the source and target point clouds must match. Conversely, point-to-function ICP and the xy-position of all points in the source point cloud from CAD were used as inputs for the surface function, and the target point cloud (surface) was calculated from the function for each iteration. Because the function is differentiable, we calculated the target xyz points and the normals from the derivative at each surface position. This makes it straightforward to calculate the point correspondence between the source and target, even when the spatial resolutions of the source and target point clouds differ.
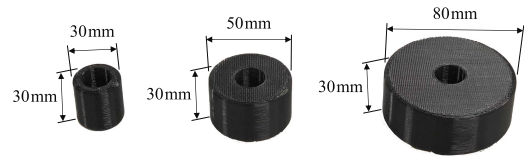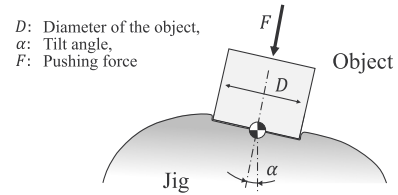
Here, the rotation around the z-axis in the objective function ε for ICP can be fixed if the object is rotationally symmetric (e.g., bearing). The objective function used in the point-to-plane and point-to-function metric is expressed as

$$\varepsilon = \sum_{i=1}^{N_p} \left[(\boldsymbol{R}\boldsymbol{p}_i + \boldsymbol{t} - \boldsymbol{q}_i) \cdot \boldsymbol{n}_i \right]^2 \tag{1}$$

where

$$\boldsymbol{R} = \begin{cases} \boldsymbol{R}_x \boldsymbol{R}_y & \text{if rotationally symmetric} \\ \boldsymbol{R}_x \boldsymbol{R}_y \boldsymbol{R}_z & \text{otherwise.} \end{cases}$$

$\boldsymbol{R}_x, \boldsymbol{R}_y, \boldsymbol{R}_z$ are the rotation matrices around the x-, y-, and z-axes in the fixed coordinate system, respectively. $\boldsymbol{R}$ is the combined rotation matrix, $\boldsymbol{t}$ is the translation vector, $\boldsymbol{p}_i$ (source), and $\boldsymbol{q}_i$ (target) are the pairs of corresponding points, $\boldsymbol{n}_i$ is the normal vector of the target, and N_p is the number of corresponding points found in the ICP. Here, we utilize a 5-DoF metric when $\boldsymbol{R}$ is $\boldsymbol{R}_x \boldsymbol{R}_y$ and a 6-DoF metric when $\boldsymbol{R}$ is $\boldsymbol{R}_x \boldsymbol{R}_y \boldsymbol{R}_z$.

We minimized this ε using the Levenberg–Marquard algorithm [23] to search for pose parameters ($\boldsymbol{R}$ and $\boldsymbol{t}$) and treated the result as the pose of the object.

V. EXPERIMENTS AND RESULTS
A. JIG COORDINATE CALIBRATION

We performed jig coordinate calibration to evaluate the pose estimation method and convert the pose acquired from the jig into a coordinate system for the robot.

For calibration, we used a manipulator (LBR iiwa 14 R820, KUKA) to precisely control the pose of the object pressed against the jig. The robot and soft jig were arranged as shown in Fig. 12. To transform the pose of the grasped object from a robot coordinate system to a jig coordinate system, a hand-eye camera and four circular markers on the jig were used for coordinate alignment. To obtain the transformation, we solved the perspective-n-point problem [24].
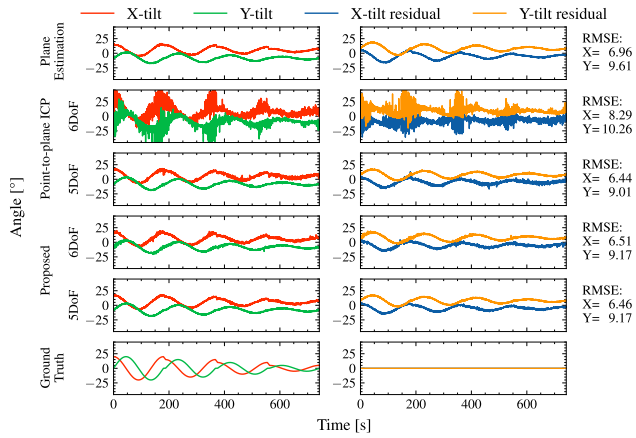
FIGURE 15. Tilt angles and residuals before calibration of cylinders with a diameter of 50 mm. The red and green lines denote the x- and y-tilts acquired from the jig, respectively, whereas the blue and orange lines denote the x- and y-tilt residuals from the ground truth, respectively.
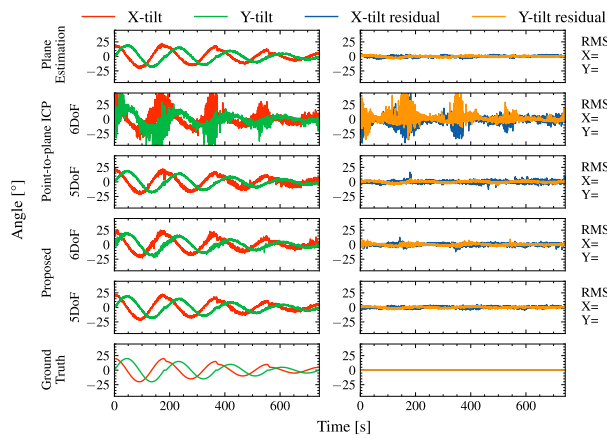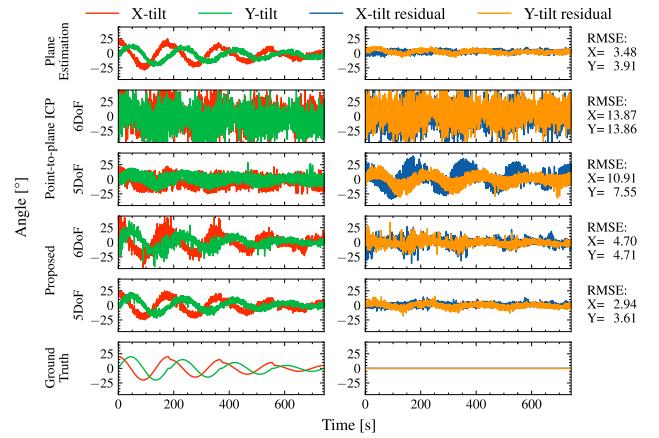

FIGURE 16. Estimated tilt angles and their residuals after calibration of a cylinder with a diameter of 50 mm.

FIGURE 17. Estimated tilt angles and its residuals after the calibration of a cylinder with a diameter of 30 mm.

FIGURE 18. Estimated tilt angles and their residuals after the calibration of a cylinder with a diameter of 80 mm.
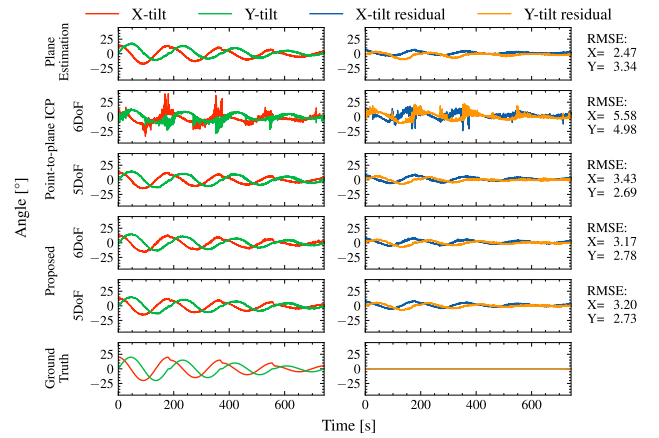
Fig. 13 shows the cylindrical objects used for calibration. The robot grasps these objects and moves to the origin within a horizontal orientation in the xy-plane of the jig coordinate system, using the marker recognized by the camera. Fig. 14 shows a diagram of the motion of the robot pressing the object. The robot presses the grasped object against the jig, and the grasped object is tilted to specified angles α; however, the tilt direction of the object was changed by 360° within a period of 1° per second without using a pump to fix the object.

While changing the pose of an object, we estimated the object orientation from the jig using plane estimation [25], a point-to-plane ICP algorithm (applied to a point cloud), and the proposed point-to-function ICP algorithm (applied to a function). Here, we apply ICP algorithms with the 6-DoF and 5-DoF metrics (without rotation around the z-axis) while considering the target objects to be cylindrical.

The x-tilt Ax and y-tilt Ay were calculated using plane estimation, the ICP algorithms, and ground truth by projecting the normal vector of the object pose onto the yz- and xz-planes and converting them into angles.

Next, we calculated three parameters (offsets O_x, O_y, and scale S) for cylinders with diameters of 50 mm as calibration results to obtain the correct value of the acquired tilt angle. Ax_j and Ay_j can be regarded as pure sine waves in the yz- and xz-planes, considering the tilt direction was changed by 360° while maintaining the angle α constant in the radial direction determined by the robot. Therefore, the offsets O_x, O_y, and the scale S can be calculated using the following equations:
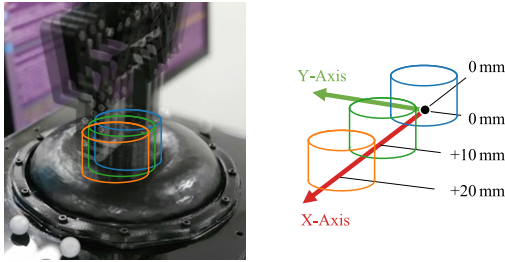
$$O_x = \frac{1}{N_s} \sum_{j=1}^{N_s} Ax_j, \qquad (2)$$

$$O_y = \frac{1}{N_s} \sum_{j=1}^{N_s} Ay_j, \qquad (3)$$

$$S = \frac{2 \times \alpha}{\sqrt{2} \times (\sigma_x + \sigma_y)}, \qquad (4)$$

where:

$$\sigma_x = \sqrt{\frac{1}{N_s} \sum_{j=1}^{N_s} (Ax_j - O_x)^2}, \qquad (5)$$

FIGURE 19. Variations of the positions that the robot pressed on the jig. The position is varied in 10 mm increments only in the x-axis direction in the jig coordinate system.

$$\sigma_y = \sqrt{\frac{1}{N_s} \sum_{j=1}^{N_s} (Ayj - O_y)^2}, \quad (6)$$

N_s is the number of samples used for calibration.

The tilt angles of a cylinder with a diameter of 50 mm acquired using plane estimation, ICP algorithms, and ground truth used as a command value to the robot are shown in Fig. 15. The tilt angles calibrated for cylinders with diameters of 50 mm using these parameters are shown in Fig. 16. The tilt angles calibrated for cylinders with diameters of 30 mm and 80 mm, using the same parameters as those of 50 mm, are shown in Fig. 17 and Fig. 18. The RMSE for the results are listed on the right in Fig. 15–18.

We observed that the planar estimation [25] and the proposed method (5-DoF) have approximately the same results and can be estimated with high accuracy at an RMSE of less than 4° in Fig. 16–18. When the diameter of the object was small, the number of markers that could be referenced was small, and the pose estimation result became noisy. This is evident from the considerable noise observed in the pose estimation results at the diameter of 30 mm, where the point-to-plane ICP method failed to produce accurate estimates. However, it is clear that the proposed method improves estimation accuracy with an RMSE more than twice as large. In addition, the noise level varied depending on the estimated degrees of freedom during the pose estimation.

At a diameter of 80 mm, the residuals were larger when the tilt was large because when a large object is tilted and pressed against the jig at a large angle, a part of the bottom surface of the object lifts and loses contact with the jig, as described in Appendix B.

B. PUSHED OBJECT POSE ESTIMATION

We performed pose estimation at various positions and angles to evaluate the pose estimation results when the pressed position was not at the center.

The robot grasps a cylinder with a diameter of 50 mm and moves the cylinder to the coordinates away from the center in 10 mm increments, as shown in Fig. 19. This cylinder was tilted around the y-axis by the robot to specific angles α of 5°, 10°, 15°, and 20° from the center of the contacting bottom. The contact with the jig was determined when the
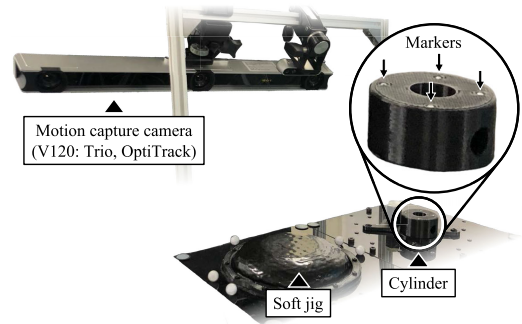
FIGURE 20. Setup to evaluate the estimation performance of the soft jig. A motion capture camera is mounted from above to capture a cylinder at various orientations and positions on the jig.
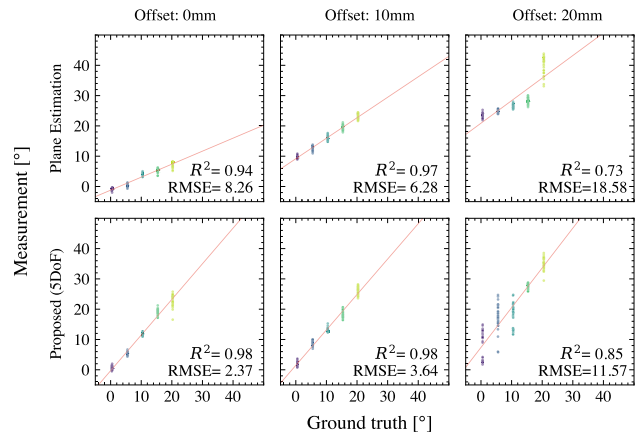
FIGURE 21. Tilt estimation results around the y-axis and the ground truth measured by motion capture when the position is varied from 0 mm to 20 mm and the angle is varied from 0° to 20°. The data are plotted for each pose for a period of 3 s. The red line denotes equal relation.
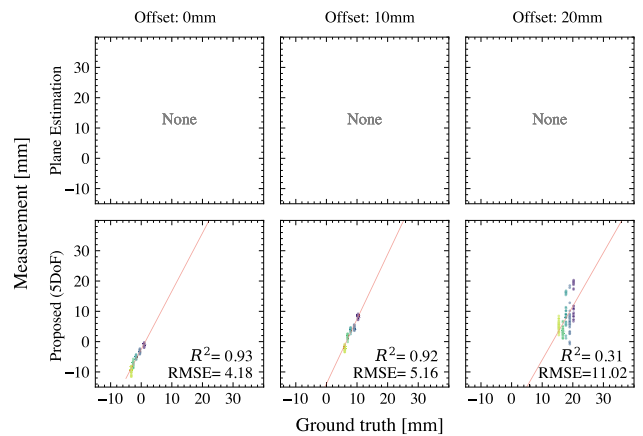
FIGURE 22. Position estimation results in the x-direction and the ground truth measured by motion capture when the position is varied from 0 mm to 20 mm, and the angle is varied from 0° to 20°. The data are plotted for each pose for a period of 3 s. The red line denotes equal relation.

force applied to the wrist of the manipulator was changed by 1 N or more. After contact detection, the robot pushed the object with a force of 5 N; the jig estimated the object pose
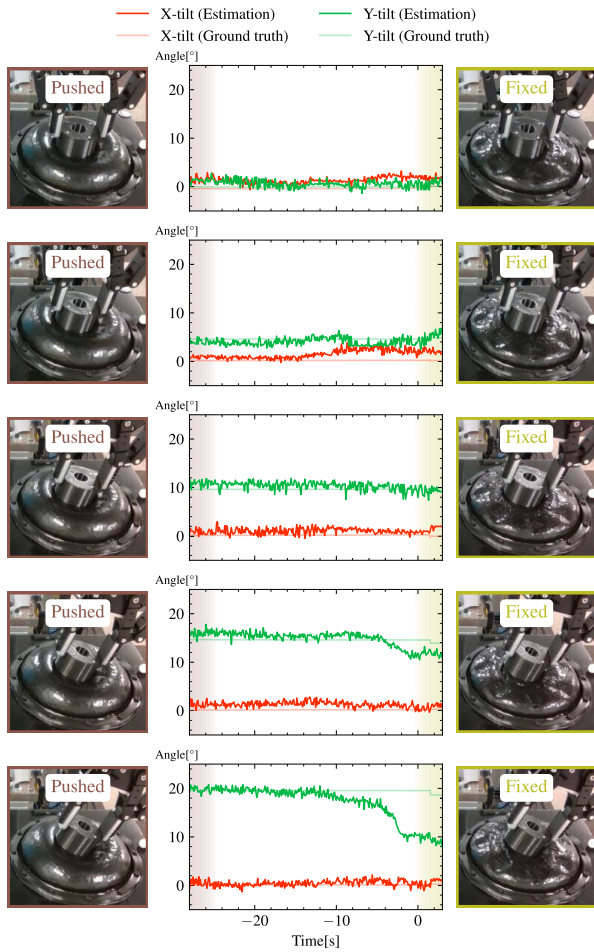
FIGURE 23. Estimated tilt angles from pressed to fixed.

FIGURE 24. Displacements from pressed to released. The minute displacement after 0.5 s was caused by vibration when the robot control was switched from force control to position control.

from the jig using plane estimation [25] and the proposed point-to-function ICP algorithm (5-DoF).

Six reflective markers on the jig and four on the cylinder were measured from the top using a motion capture system (V120: Trio, OptiTrack), as shown in Fig. 20. The y-tilt of the object determined by the jig and motion capture system was calculated by projecting the normal vector of the object pose onto the xz-planes and converting it into an angle.

The results of the tilt estimation around the y-axis are shown in Fig. 21. During planar estimation, angle errors were included in the estimates as the object moved away from the center. Additionally, when the angle of the object was large, the position of the object changed when pressed with a force of 5 N, indicating that errors occur even when the object is pressed at the center. However, the proposed method compensates for this by exploiting the fact that the estimated angle values are roughly equivalent to the ground truth at an RMSE of less than 4° and a coefficient of determination R^2 greater than 0.98, regardless of the position when the offset is between 0 mm and 10 mm. Furthermore, we confirmed that an offset larger than 20 mm includes estimation errors; however, this is
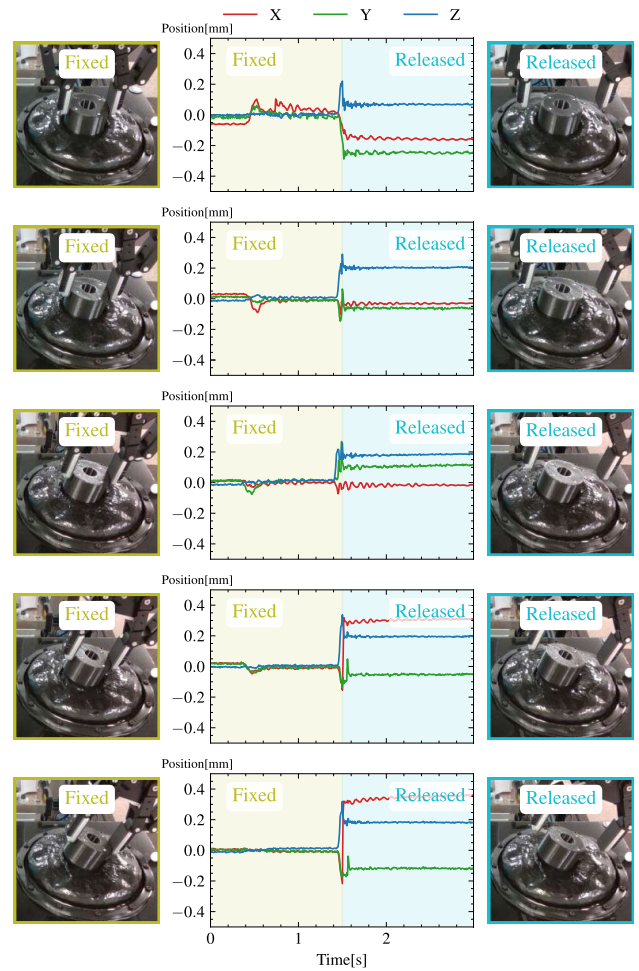
not a problem because such large positioning errors are unlikely to occur in many cases under robot control of object positions.

The position estimation results in the x-direction are shown in Fig. 22. In cases of planar estimation, the position cannot be estimated; however, in the proposed method, the position is also included in the output result. Although the deviations from the ground truth occur at an RMSE of less than 6 mm when the offset is between 0 mm and 10 mm, it is possible to correct because R^2 is higher than 0.92.

C. PLACED OBJECT FIXING

We performed an object-fixing experiment to clarify when the pose should be estimated with the jig and to analyze the fixed pose variability caused by supporting an object with a flexible material instead of a rigid material.

The setup and procedure for pushing the object were the same as those described in Section V-B. In this experiment, the object was pressed against the center of the jig only. After the robot pushed the object with a force of 5 N, a peristaltic

pump was used to fill the soft jig with oil; pumping stopped when the liquid level limit acquired from the camera was reached.

Snapshots of the robot pushing an object and after parts fixing are shown in Fig. 23. The angle was accurately estimated when the object was pressed against it; however, as the oil was pumped out for fixation, the accuracy of the estimation decreased.

Snapshots showing the after parts fixing and the robot releasing an object are displayed in Fig. 24. The results illustrating the difference between the pushed and released poses are shown in Fig. 25. The results show that the pose of the object changed slightly when the gripper was released; however, the amount was sufficiently small to be compensated for by compliance with the remote center compliance (RCC) devices.

D. FIXING FORCE

To evaluate the effectiveness of the proposed jig in securing an object with a threaded hole, we measured the rotation angle generated during screw-tightening using the jig.

For the experiment, we used an electric screwdriver (Bosch GO 2 Professional, Bosch) with various tightening torques. The preselected torque mode (PTM) of the electric screwdriver was adjusted using a torque-presetting ring. We measured the tightening torques for different PTMs using a joint torque sensor, as shown in Fig. 26. We used pre-measured PTM-1 to PTM-3 (0.25 Nm–1.03 Nm) in our experiment.

The soft jig, screwdriver, and target object were arranged as shown in Fig. 27 (a). We followed the screw-tightening procedure before and after measuring the rotation angle of the object, as depicted in Fig. 27 (b). The procedure involved fixing the target object in place using the jig, grasping the screwdriver, and tightening the screw. We used three types of objects as targets: a circular, octagonal, and square cylinder with a nut embedded in the center and markers for motion capture. The angle of rotation of the object being measured is shown in Fig. 27 (c) and was measured using motion capture to calculate the rotation angle around the z-axis.

The experiment results are shown in Fig. 28. The x-axis of the graph shows the combination of object geometry and PTM used in the experiments, and the y-axis shows the amount of object rotation when screwing was performed.

We found that the circular and octagonal cylinders rotated during screw-tightening, even with PTM-1, because their shape provided little constraint. However, the square cylinder was fixed and screw-tightened using PTM-1. When screw tightening was performed using PTM-2 and PTM-3, the object rotated significantly from PTM-3.

VI. DISCUSSION

A. PRECISE ESTIMATION

The soft jig performs object pose estimation for contacted objects by acquiring the membrane shape using optical
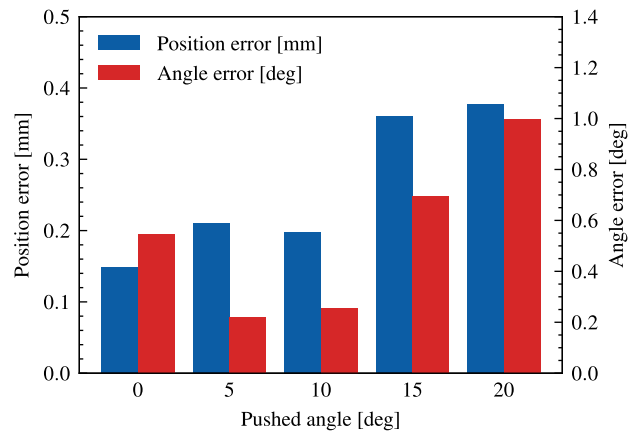
FIGURE 25. Difference between pushed and released pose. The pushed pose is the average of the 0–1 s timeframe in Fig. 24, and the released pose is the average of the 2–3 s timeframe in Fig. 24. The difference in position is the Euclidean distance between the two postures, and the difference in angle is calculated from the angular difference between the unit vectors when the unit vector is rotated by the two postures.
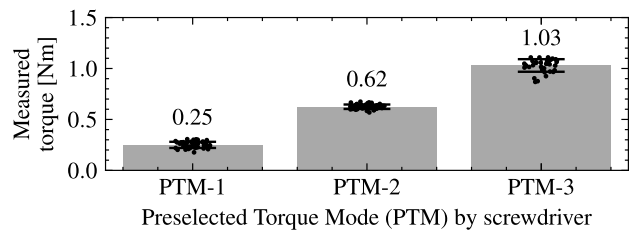
FIGURE 26. Measurement results of the torque exerted by the driver. The joint torque of the manipulator was used for the measurement.

sensing and registering the object CAD model to the membrane shape.

From the results in Section V-A, we confirmed that point-to-function ICP, which expresses the shape of the membrane as a function and estimates the object's pose, improves the accuracy. This is because the correspondence of the points can be obtained more appropriately than if the points were used directly to estimate the object pose. We also confirmed that changing the number of pose estimation parameters from 6-DoF to 5-DoF when using a cylindrical object improves the accuracy, indicating the importance of limiting the DoF of the estimation according to the object shape.

From the results in Section V-C, we confirmed that highly accurate orientation estimation can be achieved using the estimation result before fixation instead of that after fixation. The pose estimation converges correctly because the oil increases the shape difference between the object contact region and the object non-contact region.

B. HARDWARE LIMITATIONS FOR SENSING

Section V-A shows that there are limitations to the estimated allowable tilt angle and size of the soft jig. To address these limitations and improve performance, adjustments to the jig's diameter and the volume of the membrane interior may be necessary.
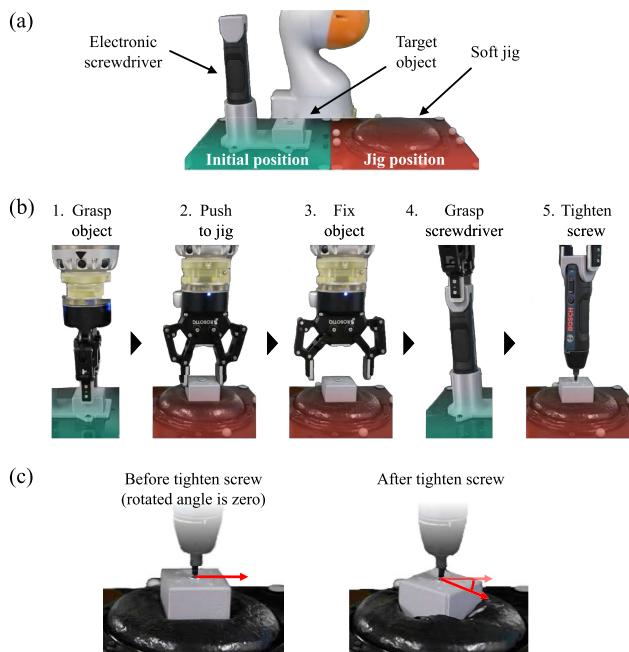
FIGURE 27. (a) Setup for the screw tightening experiment. (b) Procedure for screw tightening using a jig. (c) Angle of the object after screw tightening used for evaluation. The angle was calculated using motion capture.
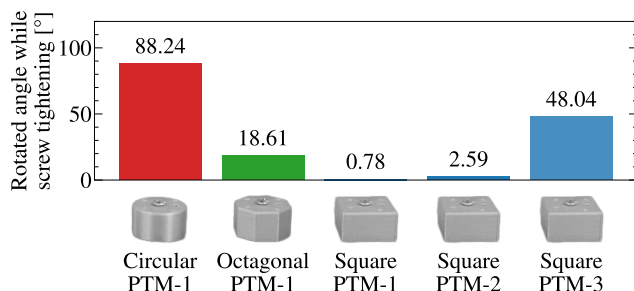
FIGURE 28. Rotation angle of the object during screw tightening. Each measurement value was calculated as the pose after the screw tightening procedure.

The current marker size of 5 mm and the distance between the markers on the membrane of approximately 10 mm pose accuracy challenges in object pose estimation. For instance, a cylinder with a diameter of 30 mm has only about seven reference markers. To enhance the accuracy, we propose reducing the marker size and distance by half, which would increase the number of reference points to 19.

Alternatively, we could improve pose estimation accuracy by introducing a mechanism that can change the membrane's color to visible or invisible, as shown in a previous study [26]. Another option would be to use multi-color illumination techniques [16], [20] to minimize the uncertainty of the pose estimation process.

C. HARDWARE LIMITATION FOR FIXING
The results in Section V-C demonstrate that the proposed jig successfully placed objects with high accuracy. Moreover,

the jig can be used for re-grasping to further improve the gripper's object grasping posture, as demonstrated in a previous study [27].

However, the results in Section V-D reveal challenges in constraining objects using the proposed jig. This is because the jig relies on a form closure, which utilizes the shape of the object to constrain it, rather than a force closure, which applies a force to constrain the object. Nevertheless, it is worth noting that the mechanical clutch was activated during screw tightening, and the screw was tightened to the specified torque. This can be attributed to the frictional effect of the flexible membrane on the jig.

VII. CONCLUSION
This paper proposed a novel soft jig inspired by jamming grippers, which uses a soft membrane containing transparent beads and oil with an adjusted refractive index to improve the efficiency of robotic assembly processes. The soft jig incorporates a hydraulic drive system for controlling the amount of oil inside the membrane and fixes the object while maintaining transparency inside the membrane. Additionally, it is equipped with a sensing system that estimates the pose of an object based on a point-to-function ICP.

Our experiments validated the proposed jig's ability to estimate the orientation of cylindrical objects between diameters of 30 mm and 80 mm by pressing objects at the center of the jig, with an RMSE of less than 4°. Furthermore, we demonstrated that the proposed method could estimate the orientation and position even if the object is not pressed at the center of the jig, provided that the amount of misalignment is 10 mm or less. These results indicate that the proposed method outperforms previously proposed sensing methods. Furthermore, in the object-fixing experiments with multiple angles (from 0° to 20°), we confirmed that the jig maintained the pose of the object at a position of less than 0.5 mm and an angle of less than 1.1°.

Combined with the object pose estimation, the jig allows us to perform precise assembly operations by re-grasping or changing the assembled object's pose to the target pose. In other words, the soft jig is an active perception jig that works with the assembly plan, unlike the conventional jigs that only fix objects in a desired pose. In the future, we intend to improve the performance of the jig, integrate the proposed jig and assembly operation planning, and work on general-purpose assembly using robots.

APPENDIX A
DIFFICULTY OF ACTUATION
In a pneumatic drive, the air is compressible and can be easily driven by a vacuum pump or other devices. Conversely, in a hydraulic drive, if oil is not output at the proper pressure and/or volume, bubbles will be generated owing to cavitation or insufficient sealing. This must be prevented because if bubbles are generated, the markers on the membrane cannot be recognized, as shown in Fig. 29.
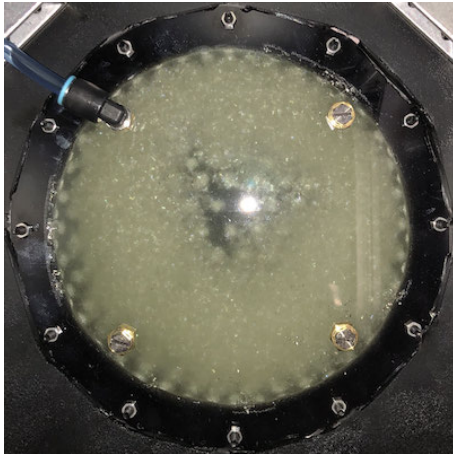
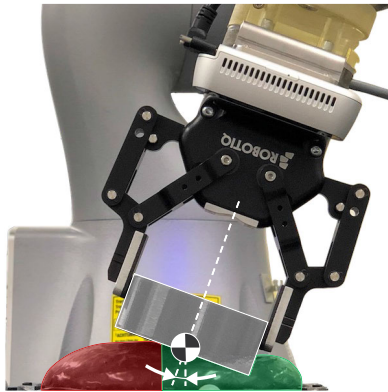**FIGURE 29. Marker visibility when air is introduced into the membrane.**

FIGURE 30. State of contact when a cylinder with a diameter of 80 mm is tilted 20°. The membrane and cylinder are in contact in the green area but not in the red area.

APPENDIX B
CONTACT STATE FOR A LARGE OBJECT

When a large object is tilted and pressed against the jig at a large angle, part of the bottom surface of the object lifts and loses contact with the jig, as shown in Fig. 30. Therefore, the object's pose cannot be accurately estimated from this membrane shape.

REFERENCES

[1] A. Gameros, S. Lowth, D. Axinte, A. Nagy-Sochacki, O. Craig, and H. R. Siller, "State-of-the-art in fixture systems for the manufacture and assembly of rigid components: A review," *Int. J. Mach. Tools Manuf.*, vol. 123, pp. 1–21, Dec. 2017.

[2] H. Asada and A. By, "Kinematic analysis of workpart fixturing for flexible assembly with automatically reconfigurable fixtures," *IEEE J. Robot. Autom.*, vol. JRA-1, no. 2, pp. 86–94, Jun. 1985.

[3] A. Mo and W. Zhang, "A novel universal gripper based on meshed pin array," *Int. J. Adv. Robotic Syst.*, vol. 16, no. 2, pp. 1–12, 2019.

[4] P. Shi, Z. Hu, K. Nagata, W. Wan, Y. Domae, and K. Harada, "Development of a shape-memorable adaptive pin array fixture," *Adv. Robot.*, vol. 35, no. 10, pp. 591–602, May 2021.

[5] J. W. Park, J. Park, H. Kim, N. Kim, and D. Y. Kim, "Assembly part positioning on transformable pin array fixture by active pin maximization and joining point alignment," *IEEE Trans. Autom. Sci. Eng.*, vol. 19, no. 2, pp. 1047–1057, Apr. 2022.

[6] T. Kiyokawa, T. Sakuma, J. Takamatsu, and T. Ogasawara, "Soft-jig-driven assembly operations," in *Proc. IEEE Int. Conf. Robot. Autom. (ICRA)*, May 2021, pp. 3466–3472.

[7] G. Du, K. Wang, S. Lian, and K. Zhao, "Vision-based robotic grasping from object localization, object pose estimation to grasp estimation for parallel grippers: A review," *Artif. Intell. Rev.*, vol. 54, no. 3, pp. 1677–1734, Mar. 2021.

[8] M. Q. Mohammed, K. L. Chung, and C. S. Chyi, "Review of deep reinforcement learning-based object grasping: Techniques, open challenges, and recommendations," *IEEE Access*, vol. 8, pp. 178450–178481, 2020.

[9] E. Brown, N. Rodenberg, J. Amend, A. Mozeika, E. Steltz, M. R. Zakin, H. Lipson, and H. M. Jaeger, "Universal robotic gripper based on the jamming of granular material," *Proc. Nat. Acad. Sci. USA*, vol. 107, no. 44, pp. 18809–18814, Nov. 2010.

[10] T. Sakuma, F. Von Drigalski, M. Ding, J. Takamatsu, and T. Ogasawara, "A universal gripper using optical sensing to acquire tactile information and membrane deformation," in *Proc. IEEE/RSJ Int. Conf. Intell. Robots Syst. (IROS)*, Oct. 2018, pp. 1–9.

[11] T. Sakuma, E. Phillips, G. A. G. Ricardez, M. Ding, J. Takamatsu, and T. Ogasawara, "A parallel gripper with a universal fingertip device using optical sensing and jamming transition for maintaining stable grasps," in *Proc. IEEE/RSJ Int. Conf. Intell. Robots Syst. (IROS)*, Nov. 2019, pp. 5814–5819.

[12] S. Lu, Z. Ahmad, M. Zoppi, X. Ding, D. Zlatanov, and R. Molfino, "Design and testing of a highly reconfigurable fixture with lockable robotic arms," *J. Mech. Des.*, vol. 138, no. 8, pp. 1–8, Aug. 2016.

[13] R. Muller, M. Esser, and M. Vette, "Reconfigurable handling systems as an enabler for large components in mass customized production," *J. Intell. Manuf.*, vol. 24, no. 5, pp. 977–990, Oct. 2013.

[14] G. Levi, Y. Golan, and A. Shapiro, "SIMJig—Smart independent minimalist jig," *IEEE Robot. Autom. Lett.*, vol. 7, no. 2, pp. 3396–3403, Apr. 2022.

[15] A. Rubio-Mateos, M. Casuso, A. Rivero, E. Ukar, and A. Lamikiz, "Vibrations characterization in milling of low stiffness parts with a rubber-based vacuum fixture," *Chin. J. Aeronaut.*, vol. 34, no. 6, pp. 54–66, Jun. 2021.

[16] W. Yuan, S. Dong, and E. Adelson, "GelSight: High-resolution robot tactile sensors for estimating geometry and force," *Sensors*, vol. 17, no. 12, p. 2762, Nov. 2017.

[17] A. Alspach, K. Hashimoto, N. Kuppuswamy, and R. Tedrake, "Soft-bubble: A highly compliant dense geometry tactile sensor for robot manipulation," in *Proc. 2nd IEEE Int. Conf. Soft Robot. (RoboSoft)*, Apr. 2019, pp. 597–604.

[18] N. Kuppuswamy, A. Alspach, A. Uttamchandani, S. Creasey, T. Ikeda, and R. Tedrake, "Soft-bubble grippers for robust and perceptive manipulation," in *Proc. IEEE/RSJ Int. Conf. Intell. Robots Syst. (IROS)*, Oct. 2020, pp. 9917–9924.

[19] X. Lin, L. Willemet, A. Bailleul, and M. Wiertlewski, "Curvature sensing with a spherical tactile sensor using the color-interference of a marker array," in *Proc. IEEE Int. Conf. Robot. Autom. (ICRA)*, May 2020, pp. 603–609.

[20] S. Li, X. Yin, C. Xia, L. Ye, X. Wang, and B. Liang, "TaTa: A universal jamming gripper with high-quality tactile perception and its application to underwater manipulation," in *Proc. Int. Conf. Robot. Autom. (ICRA)*, May 2022, pp. 6151–6157.

[21] J. M. Gómez–Paccapelo, A. A. Santarossa, H. D. Bustos, and L. A. Pugnaloni, "Effect of the granular material on the maximum holding force of a granular gripper," *Granular Matter*, vol. 23, no. 1, pp. 1–6, Feb. 2021.

[22] J. Amend, N. Cheng, S. Fakhouri, and B. Culley, "Soft robotics commercialization: Jamming grippers from research to product," *Soft Robot.*, vol. 3, no. 4, pp. 213–222, Dec. 2016.

[23] J. J. More, "The Levenberg–Marquardt algorithm: Implementation and theory," in *Numerical Analysis*. Berlin, Germany: Springer, 1978, pp. 105–116.

[24] V. Lepetit, F. Moreno-Noguer, and P. Fua, "EPnP: An accurate O(n) solution to the PnP problem," *Int. J. Comput. Vis.*, vol. 81, no. 2, pp. 155–166, Feb. 2009.

[25] T. Sakuma, T. Kiyokawa, J. Takamatsu, T. Wada, and T. Ogasawara, "Soft-jig: A flexible sensing jig for simultaneously fixing and estimating orientation of assembly parts," in *Proc. Int. Conf. Robot. Autom. (ICRA)*, May 2022, pp. 10945–10950.

[26] F. R. Hogan, M. Jenkin, S. Rezaei-Shoshtari, Y. Girdhar, D. Meger, and G. Dudek, "Seeing through your skin: Recognizing objects with a novel visuotactile sensor," in *Proc. IEEE Winter Conf. Appl. Comput. Vis. (WACV)*, Jan. 2021, pp. 1217–1226.

[27] Z. Hu, W. Wan, K. Koyama, and K. Harada, "Reducing uncertainty using placement and regrasp planning on a triangular corner fixture," *IEEE Trans. Autom. Sci. Eng.*, early access, Jan. 10, 2023, doi: 10.1109/TASE.2023.3234047.

TATSUYA SAKUMA (Member, IEEE) received the B.E. degree from the Kobe City College of Technology, Japan, and the M.E. degree from the Nara Institute of Science and Technology, Japan, in 2019. He is currently with Panasonic Holdings Corporation. His research interests include soft robotics and tactile sensors for dexterous manipulations.
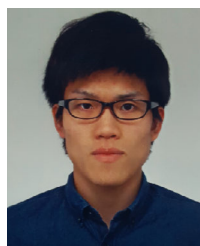
TAKUYA KIYOKAWA (Member, IEEE) received the Ph.D. degree in information science from the Nara Institute of Science and Technology, Japan, in 2021. Since 2021, he has been an Assistant Professor with Osaka University, Japan, and the Nara Institute of Science and Technology, Japan. His current research interest includes agile reconfigurable robot systems.

TAKAMITSU MATSUBARA (Member, IEEE) received the Ph.D. degree in information science from the Nara Institute of Science and Technology, Nara, Japan, in 2007. From 2005 to 2007, he was a Research Fellow (DC1) of the Japan Society for the Promotion of Science. From 2013 to 2014, he was a Visiting Researcher with the Donders Institute for Brain Cognition and Behavior, Radboud University Nijmegen, Nijmegen, The Netherlands. He is currently a Professor with the Nara Institute of Science and Technology and a Visiting Researcher with ATR, Kyoto, Japan, and the AIST AI Center, Tokyo, Japan. His current research interests include machine learning and control theory for robotics.

JUN TAKAMATSU (Member, IEEE) received the Ph.D. degree in computer science from The University of Tokyo, Japan, in 2004. From 2004 to 2008, he was with the Institute of Industrial Science, The University of Tokyo. In 2007, he was a Visiting Researcher with Microsoft Research Asia. From 2008 to 2020, he was an Associate Professor with the Nara Institute of Science and Technology, Japan. He was a Visitor with Carnegie Mellon University, from 2012 to 2013. He was a Visiting Scientist with Microsoft, in 2018, where he is currently a Senior Researcher of applied robotics. His current research interests include robotics, including learning-from-observation, task and motion planning, feasible motion analysis, 3D-shape modeling and analysis, and physics-based vision. He is a member of RSJ.

TAKAHIRO WADA (Member, IEEE) received the B.S. degree in mechanical engineering, the M.S. degree in information science and systems engineering, and the Ph.D. degree in robotics from Ritsumeikan University, Japan, in 1994, 1996, and 1999, respectively. In 1999, he was a Research Associate with Ritsumeikan University. In 2000, he joined as an Assistant Professor with the Department of Intelligent Mechanical Systems Engineering, Kagawa University, where he was promoted as an Associate Professor, in 2003. In 2006 and 2007, he spent half a year with the University of Michigan Transportation Research Institute, Ann Arbor, as a Visiting Researcher. He joined as a Full Professor with the College of Information Science and Engineering, Ritsumeikan University, in 2012. Since 2021, he has been a Full Professor and the Director of the Human Robotics Laboratory, Division of Information Science, Nara Institute of Science and Technology (NAIST), Japan. His current research interests include robotics, human–machine systems, and human modeling. He is a member of IEEE ITSS, IEEE SMC, IEEE RAS, the Robotics Society of Japan, Society for Neuroscience, the Society of Automotive Engineers of Japan, and the Society of Instrument and Control Engineers (SICE). He received the Best Paper Award from JSAE, in 2008 and 2011, and the Outstanding Oral Presentation from the Society for Automotive Engineers (SAE), in 2010.

TSUKASA OGASAWARA (Life Member, IEEE) received the Ph.D. degree from The University of Tokyo, Japan, in 1983. From 1983 to 1998, he was with the Electrotechnical Laboratory, Ministry of International Trade and Industry, Japan. From 1993 to 1994, he was with the Institute for Real-Time Computer Systems and Robotics, University of Karlsruhe, Germany, as a Humboldt Research Fellow. He joined the Nara Institute of Science and Technology, Nara, Japan, in 1998, where he has been with the Robotics Laboratory, until March 2021. He is currently the Executive Director and the Vice President of the Nara Institute of Science and Technology. His research interests include human–robot interaction, dexterous manipulation, human modeling, and bio-inspired robotics.

• • •